Pergamon

0956-7151(93)E0068-E

Acta metall. mater. Vol. 42, No. 5, pp. 1683–1693, 1994
Elsevier Science Ltd
Printed in Great Britain
0956-7151/94 $6.00 + 0.00

A MODEL FOR MICROCRACK INITIATION AND PROPAGATION BENEATH HERTZIAN CONTACTS IN POLYCRYSTALLINE CERAMICS

B. R. LAWN, N. P. PADTURE†, F. GUIBERTEAU‡ and H. CAI†

Materials Science and Engineering Laboratory, National Institute of Standards and Technology, Gaithersburg, MD 20899, U.S.A.

(Received 27 September 1993)

Abstract—A fracture mechanics model of damage evolution within Hertzian stress fields in heterogeneous brittle ceramics is developed. Discrete microcracks generate from shear faults associated with the heterogeneous ceramic microstructure; e.g. in polycrystalline alumina, they initiate at the ends of intragrain twin lamellae and extend along intergrain boundaries. Unlike the well-defined classical cone fracture that occurs in the weakly tensile region *outside* the surface contact in homogeneous brittle solids, the fault-microcrack damage in polycrystalline ceramics is distributed within a subsurface shear-compression zone *below* the contact. The shear faults are modelled as sliding interfaces with friction, in the manner of established rock mechanics descriptions but with provision for critical nucleation and matrix restraining stresses. This allows for constrained microcrack pop-in during the loading half-cycle. Ensuing stable microcrack extension is then analyzed in terms of a K-field formulation. For simplicity, only mode I extension is considered specifically here, although provision exists for including mode II. The compressive stresses in the subsurface field constrain microcrack growth during the loading half-cycle, such that enhanced extension occurs during unloading. Data from damage observations in alumina ceramics are used to illustrate the theoretical predictions. Microstructural scaling is a vital element in the microcrack description: initiation is unstable only above a critical grain size, and extension increases as the grain size increases. Internal residual stresses also play an important role in determining the extent of microcrack damage. Implications of the results in the practical context of wear and fatigue properties are discussed.

1. INTRODUCTION

The nature of contact damage beneath an indenting sphere on a brittle surface has been extensively studied in homogeneous, isotropic materials like glasses and single crystals, and in some fine-grain ceramics. In such relatively ideal materials one observes an elastic response up to a critical load, whence a classical "Hertzian cone fracture" suddenly develops outside the contact circle [1–8]. Traditional cone fractures tend to be near-symmetrical and well-defined, and are accordingly amenable to linear elastic fracture mechanics analysis [3]. On the other hand, it is possible under certain circumstances (e.g. softer materials, harder and smaller indenters) to suppress the cone fracture and to induce subsurface deformation, thereby providing information on intrinsic deformation processes in otherwise highly brittle solids [9, 10].

Given this background, it is perhaps surprising that relatively little attention has been given to the nature of Hertzian damage in heterogeneous polycrystalline ceramics. This is especially so in those coarser ceramics where weak interfaces and internal stresses exert a controlling influence on the fracture process, leading to countervailing "toughness-curve" (T-curve, or R-curve) effects [11]. Thus, whereas the toughness in the *long*-crack region is enhanced by grain-interlock bridging [12–16], in the *short*-crack region it is diminished by thermal expansion mismatch stresses at tensile grain or interphase boundaries [15]. Recently, spherical indenter tests on a coarse-grain alumina [17, 18] and a glass–ceramic [19] have revealed a different kind of contact damage, with the following distinctive features:

- (i) A well-defined "indentation stress–strain" curve, independent of sphere size, indicating a deviation from the ideal Hertzian elasticity relations toward a "plastic contact" at high indentation pressures.
- (ii) Instead of the classical cone fracture *outside* the contact circle, where the stresses are (weakly) tensile, a microfracture initiation and coalescence zone *beneath* the contact circle, where the stresses are (strongly) hydrostatic compressive and deviatoric in nature.
- (iii) An indication that each microfracture is preceded by some kind of stress-concentrating

---

†Guest Scientist, from Department of Materials Science and Engineering, Lehigh University, Bethlehem, PA 18015, U.S.A.

‡Guest Scientist, from Departamento de Física, Universidad de Extremadura, 06071-Badajoz, Spain.

> "constrained shear fault" (e.g. twin lamella, in the case of alumina), so that the damage is intrinsic to the microstructure.

In addition, the damage zone expands in repeat contacts, with progressive microcrack coalescence and ultimate material removal, indicating a true mechanical fatigue effect. Such features are of special interest to those concerned with the strength, fatigue and wear of structural ceramics.

In this paper we present a generic fracture mechanics model of the microfracture evolution within the subsurface damage zone in polycrystalline ceramics during a full indentation loading and unloading cycle. The crux of our model is the initiation and subsequent growth of a microcrack from some shear fault within the compressive indentation zone. This evolution is described in terms of a detailed K-field formulation [11]. The envisaged process is loosely based on the "pile-up" concept for crack initiation in semi-brittle solids [11, 20–22]. The process is also reminiscent of the kind of crack initiation that occurs beneath "sharp" (e.g. Vickers) indenters in glasses [23, 24], in rocks and other coarse-grain materials subjected to macroscopic confining pressures [25–29], and in compressively loaded notched ceramics [30–32]. In setting up our model we shall borrow from these earlier research areas, although new elements specifically pertinent to structural ceramics will also be introduced. The scale of individual damage events is determined by a characteristic microstructural dimension, grain size in the case of polycrystalline alumina, which limits the length of the critical shear fault and thereby determines threshold conditions for microcracking. Ideally, the microcracks are assumed to propagate along constrained grain boundaries or other weak interfaces in predominantly extensile mode (i.e. mode I). These microcracks are, by virtue of the compressive nature of the immediate subsurface contact field, highly stable in their subsequent evolution, with continued propagation during unloading. In actuality, the geometrical constraints imposed by the grain boundaries relative to the shear fault and Hertzian field will inevitably result in superposed shear stresses on the microcrack surfaces (i.e. mode II), opening the way to frictional tractions and hence hysteresis during unloading–reloading cycles, i.e. fatigue.

In the interest of mathematical simplicity, we confine ourselves here to mode I microcrack extension. Data from previous studies on polycrystalline alumina will be used to illustrate how one may calibrate K-field parameters in the analysis, and thence evaluate the microcrack development through a complete Hertzian load–unload cycle. In particular, we address the important role of grain size, in special relation to the crack initiation (pop-in) and subsequent propagation. We shall determine that a greater portion of the propagation actually takes place during the unloading half-cycle, although in a highly stable manner.

Whereas we specifically address single-cycle, mode I microfracture here, we foreshadow potential extension of the model to fatigue and wear properties by inclusion of mode II frictional tractions at the closed microcrack interfaces. The mode II component allows for hysteresis in cyclic loading, enabling progressive coalescence of neighboring microcracks and, ultimately, material removal.

2. NATURE OF DAMAGE IN HERTZIAN CONTACT FIELD

2.1. Background experimental observations on polycrystalline alumina

The nature of Hertzian contact damage on polycrystalline ceramics has been examined in recent experimental studies on alumina [17, 18] and glass–ceramics [19]. From these studies we identify the following features:

(i) Macroscopically, the damage occurs in a region of intense hydrostatic compression and shear stress, reminiscent of the deformation observed in homogeneous brittle solids in sharp-indenter fields [10, 33–37] and in rocks under confining pressures [25–27]. The extent of deformation can be quantified by departure from the linear Hertzian elasticity relation on an indentation stress–strain diagram, mean contact pressure $p_0 = P/\pi a^2$ vs contact strain a/r [9, 10, 38]. For polycrystalline alumina in Fig. 1 [18], we see that this curve is independent of grain size, indicating a material "yield stress". Note the relatively high values of p_0, up to 10 GPa, typical of contact configurations.

(ii) Microscopically, the contact deformation is associated with the activation of discrete "shear faults", from which microcracks initiate. It is implicit that the shear fault is obstructed in its extension, e.g. by intersection with weak grain boundaries, to

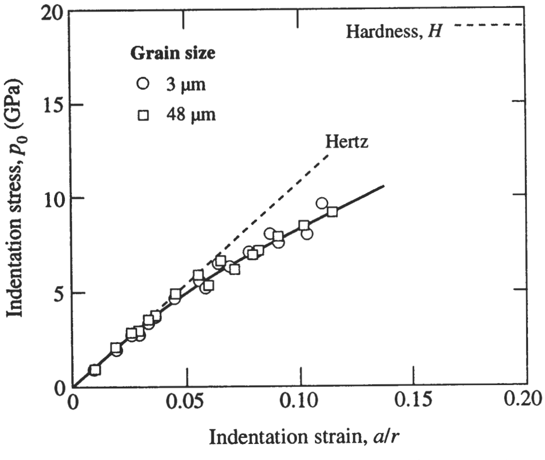

Fig. 1. Indentation stress–strain curve for aluminas, obtained using tungsten carbide (WC) spheres of radius $r = 1.98$–12.70 mm. Inclined dashed line is Hertzian elastic response and upper horizontal dashed line is Vickers hardness (averaged over all grain sizes). Solid curve is an empirical fit to the data. (After [18].)

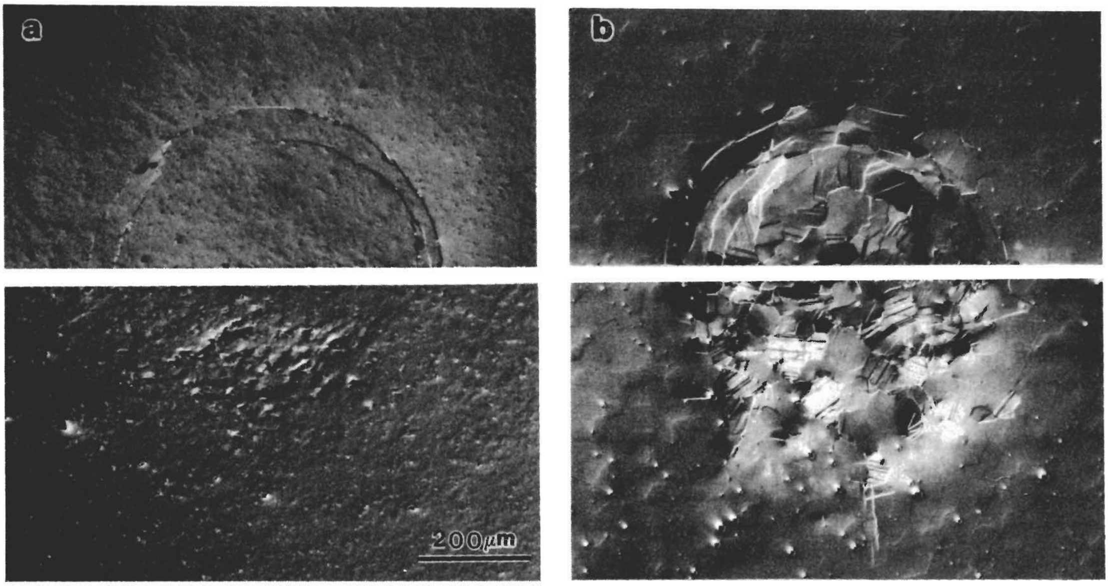

Fig. 2. Optical micrographs in Nomarski illumination showing half-surface (top) and section (bottom) views of indentation sites in aluminas, grain size (a) 9 μm and (b) 48 μm. Indentations made at indentation pressure $p_0 = 8.0$ GPa, using WC sphere of radius $r = 3.18$ mm at load $P = 2000$ N. (After [18].)

produce a local stress concentration [11, 20]. We show representative section views in Fig. 2(a) and 2(b) for aluminas of two grain sizes, "fine" (9 μm) and "coarse" (48 μm), at a contact pressure in the nonlinear indentation stress–strain region. In the fine-grain material we see limited subsurface microcrack damage (section view), along with classical cone crack traces (half-surface view). The extent of subsurface microcracking is much more apparent in the coarse-grain material. In alumina, the shear faults are principally identifiable as intra-grain twins, clearly visible in Fig. 2(b) [17]. Acoustic emission data from load–unload indentation cycles on a broad range of aluminas in Fig. 3 indicates a pronounced increase in damage activity above a grain size $\approx 20\,\mu$m. Note that the bulk of the activity occurs above a contact pressure ≈ 5 GPa during the loading half-cycle.

The features outlined in (i) and (ii) are generic to brittle materials, apart from the underlying sources of the shear faults, which are material-specific (see Section 6).

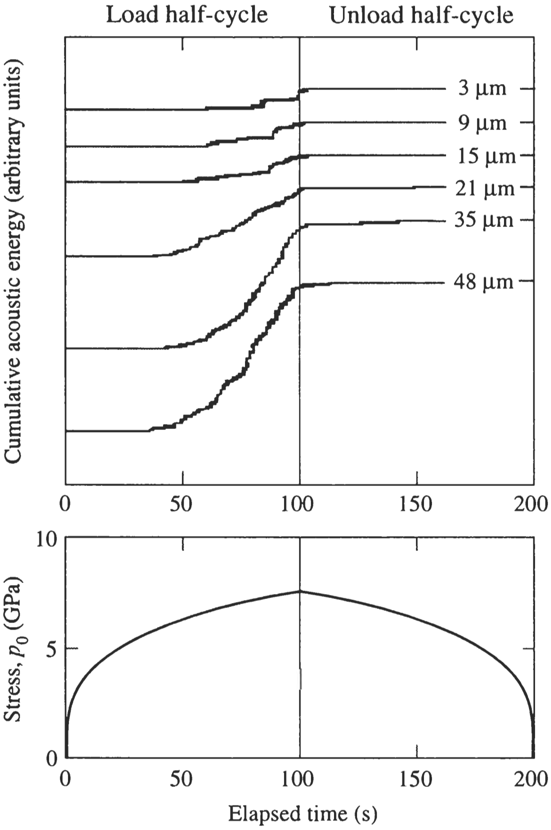

Fig. 3. Plots of cumulative acoustic energy (arbitrary linear scale) vs elapsed time during single load–unload indentation cycle (constant crosshead speed) in alumina specimens (upper diagram), using WC sphere of radius $r = 3.18$ mm. Variation of contact pressure with time indicated (lower diagram). (After [18].)

2.2. Stress field considerations

In this subsection we summarize the pertinent characteristics of the Hertzian elastic contact field [3, 6, 39]. The confining principal normal stresses σ_1, σ_2 and σ_3 within the prospective damage zone prior to deformation are so defined that $\sigma_1 > \sigma_2 > \sigma_3$ nearly everywhere (positive stress tensile). Beneath the indentation center the trajectory of maximum compression $-\sigma_3$ runs parallel to the contact axis, and that of minimum compression $-\sigma_1$ (or $-\sigma_2$)

runs perpendicular to that axis. Figure 4 shows contours of principal normal stresses σ_1 and σ_3 and principal shear stress $\frac{1}{2}(\sigma_1 - \sigma_3)$, here plotted for Poisson's ratio $\nu = 0.22$ (appropriate to alumina). In these plots the contact radius a determines the spatial scale, and contact pressure p_0 the intensity, of the stress field. The tensile stresses $+\sigma_1$, Fig. 4(a), are relatively weak, with a maximum $0.28p_0$ *at* the contact circle and rapid falloff *outside* the contact circle. The shear stresses, Fig. 4(c), are stronger, with maximum $0.49p_0$ along the contact axis at depth $\approx 0.5a$ on planes oriented at 45° to this axis; they are less concentrated than their tensile counterparts, and are confined within a zone of high biaxial hydrostatic compression, $\frac{1}{2}(\sigma_1 + \sigma_3)$.

The damage in Fig. 2 takes place almost exclusively within a drop-shaped zone below the contact, and begins subsurface, indicating that it is the maximum shear stress that primarily initiates the damage [17]. This is in striking contrast with the traditional cone fracture which, we recall, initiates and propagates in the tensile region outside the contact circle in Fig. 4(a) [3, 40]. Of course, once damage does occur the field is no longer purely elastic. However, provided we concern ourselves primarily with conditions for the onset of microcracking from individual shear faults rather than with subsequent damage coalescence and evolution into a full "plastic" zone [38], the Hertzian field may be retained as a useful base for fracture mechanics calculations.

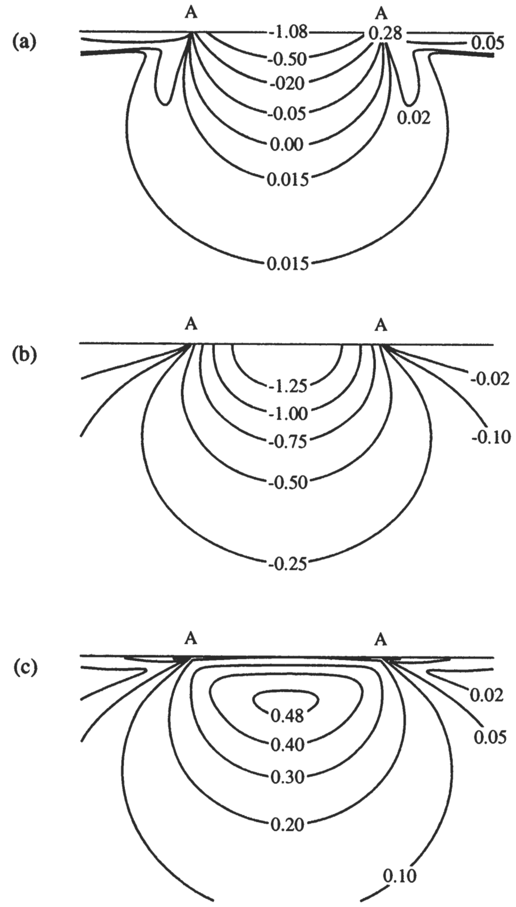

Fig. 4. Stress contours in Hertzian contact field, normalized to p_0. AA denotes contact diameter $2a$. (a) Maximum principal normal stress σ_1, (b) minimum principal normal stress σ_3, and (c) principal shear stress $\frac{1}{2}(\sigma_1 - \sigma_3)$. Note region of high biaxial hydrostatic compression $\frac{1}{2}(\sigma_1 + \sigma_3)$ beneath contact. Calculated using Poisson's ratio $\nu = 0.22$ for alumina.

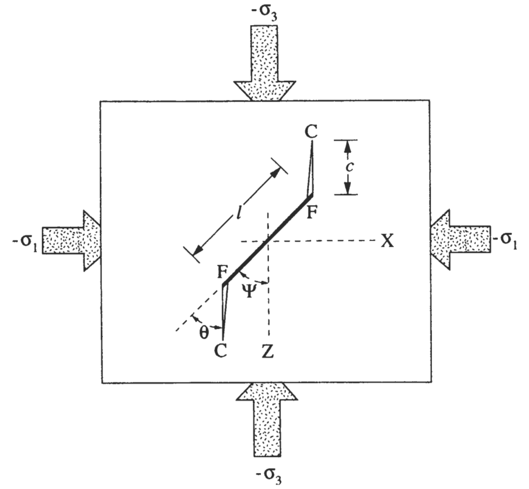

Fig. 5. Deformation-microfracture damage in polycrystalline ceramic, grain size l. Volume element is subjected to compressive normal stresses $-\sigma_1$ and $-\sigma_3$ along contact axis below spherical indenter. Shear stresses initiate intragrain slip bands FF, from which intergrain extensile microcracks FC extend at their constrained ends.

In accordance with these considerations, we set up the model for microcrack initiation shown in Fig. 5. An incipient shear fault FF is contained in a volume element beneath a spherical indenter in a material of grain size l (Section 3). At their ends the faults are constrained by some microstructural interface, e.g. weak grain boundary, along which microcracks FC ultimately initiate (Section 4). We do not specify the *nature* of the fault, so the model is generic: however, we do specify that the *scale* of the fault is determined by l. In the limit of sufficiently large contacts, $l \ll a$, uniform normal and shear contact stresses

$$\sigma(\Psi) = \tfrac{1}{2}(\sigma_1 + \sigma_3) + \tfrac{1}{2}(\sigma_1 - \sigma_3)\cos 2\Psi \qquad (1a)$$

$$\tau(\Psi) = \tfrac{1}{2}(\sigma_1 - \sigma_3)\sin 2\Psi \qquad (1b)$$

act on the fault plane, where Ψ is the angle between the fault and the σ_3 trajectory. We see directly from eqn. 1b that the fault orientation for maximum shear stress is $\Psi \approx 45°$, as pictured in Fig. 5. The corresponding stresses acting on the extended microcrack plane are

$$\sigma(\Psi - \theta) = \tfrac{1}{2}(\sigma_1 + \sigma_3) + \tfrac{1}{2}(\sigma_1 - \sigma_3)\cos 2(\Psi - \theta) \qquad (2a)$$

$$\tau(\Psi - \theta) = \tfrac{1}{2}(\sigma_1 - \sigma_3)\sin 2(\Psi - \theta). \qquad (2b)$$

Note that in the favored orientation $\Psi \approx \theta \approx 45°$ [28, 29], the shear component in equation (2b) tends to zero.

In typical ceramics, internal mismatch stresses also act at individual grain boundaries, some tensile and some compressive. Predominant in noncubic monophase and two-phase materials are those residual stresses, σ_R, due to thermal expansion mismatch. In alumina these stresses have a value $\sigma_R \approx 200$ MPa [16, 41], i.e. more than an order of magnitude lower than the contact stresses $p_0 \approx 5$–10 GPa in the deformation region of Fig. 1. Microcracks that initiate on tensile grain facets are more likely than those on compressive facets to extend into adjacent grain boundaries. Those extending microcracks that ultimately coalesce with their neighbors (e.g. from contact overloading, fatigue from cyclic loading, or chemical enhancement) will become increasingly subject to sliding friction tractions across the crack interface at adjacent compressive facets, resulting in a progressively increasing toughness by bridging (toughness-curve, or T-curve, behavior) [15]. We shall regard such bridging tractions as secondary elements in the micromechanics in this study.

3. SHEAR-FAULT MICROMECHANICS

Now consider the conditions for activation of the closed shear fault FF in Fig. 5. To do this we resort to the phenomenological constitutive relations adopted by rock mechanists [25, 26], whereby the sliding faces of the fault are subject to resistive tractions. We acknowledge that the normal (N) contact field stresses on the fault (F) plane in the subsurface damage zone will usually be compressive by defining

$$\sigma_F^N = \sigma(\Psi) = -\alpha_F p_0 \tag{3}$$

with $\alpha_F = -\sigma(\Psi)/p_0$ a positive coefficient (p_0 positive). The applied shear (S) stress on the sliding fault will be resisted by internal stresses from the intrinsic cohesion (e.g. twinning stress), τ_F, and frictional sliding, $\mu_F \sigma_F^N$, where μ_F is a fault friction coefficient. Thus, again with due allowance for the negative sign of σ_F^N, and for sign reversal of the resistance stresses on unloading, the net shear stress may be written [25]

$$\begin{aligned}\sigma_F^S &= |\tau(\Psi)| + \mu_F \sigma(\Psi) - \tau_F \\ &= (\beta_F - \alpha_F \mu_F) p_0 - \tau_F, \quad \text{(forward slip)} \end{aligned} \tag{4a}$$

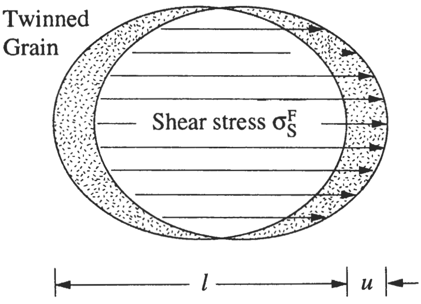

Fig. 6. Twinning slip of grain across shear plane at stress σ_F^S, resulting in strain u/l.

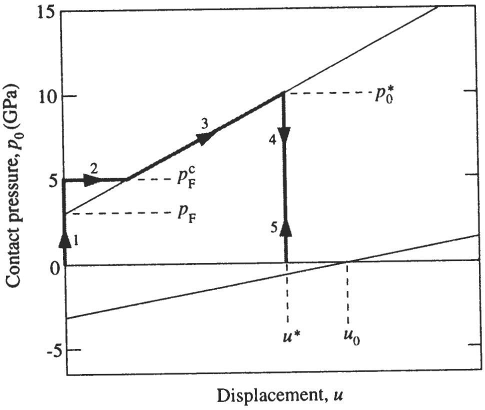

Fig. 7. Plots showing shear displacement u for twinned grain at location of maximum shear stress in Hertzian field at pressure p_0. (Pressure axis "calibrated" from alumina data in Section 5.) Case shown corresponds to zero reverse slip, $u^* < u_0$.

$$\begin{aligned}\sigma_F^S &= |\tau(\Psi)| - \mu_F \sigma(\Psi) + \tau_F \\ &= (\beta_F + \alpha_F \mu_F) p_0 + \tau_F, \quad \text{(backward slip)} \end{aligned} \tag{4b}$$

with $\beta_F = |\tau(\Psi)|/p_0$ another positive coefficient. Note that invariance of the coefficients α_F and β_F through the indentation cycle is contingent on complete reversibility of the stress field.

Accordingly, a necessary requirement for faulting to occur is that $\sigma_F^S > 0$ in equation (4). Where the fault interface has low cohesion but is rough (e.g. debonded interfaces in certain particle–matrix composites), the frictional term will dominate the mechanics. Where the fault must first be initiated (e.g. twinning in alumina), the cohesion term will dominate. In the latter case provision may be necessary to allow for a barrier to fault initiation, e.g. by defining a critical nucleation cohesion stress $\tau_F^c > \tau_F$.

Continued sliding of the fault within a grain confined in the Hertzian field is opposed by the surrounding elastic matrix, which exerts a linear restraining force in proportion to the shear displacement u, Fig. 6. At equilibrium

$$\sigma_F^S = \kappa u \tag{5}$$

where κ is an elastic stiffness term. We may now combine equations (4) and (5) for the contact pressure p_0 as a function of displacement u to produce constitutive equilibrium relations for our shear fault

$$p_0 = (\kappa u + \tau_F)/(\beta_F - \alpha_F \mu_F), \text{ (forward slip)} \tag{6a}$$

$$p_0 = (\kappa u - \tau_F)/(\beta_F + \alpha_F \mu_F), \text{ (backward slip).} \tag{6b}$$

A plot of the function $p_0(u)$ from equation (6) is shown in Fig. 7. In this plot the upper inclined line represents equation (6a), with slope $\kappa/(\beta_F - \alpha_F \mu_F)$ and intercept $\tau_F/(\beta_F - \alpha_F \mu_F)$ on the p_0 axis. Similarly, the lower inclined line represents equation (6b), with slope $\tau_F/(\beta_F - \alpha_F \mu_F)$ and intercept $-\tau_F/(\beta_F + \alpha_F \mu_F)$. The vertical dashed line at $u_0 = \tau_F/\kappa$ represents the intersection of equation (6b) with the u axis.

Consider the potential response for load–unload contact cycles, indicated in the plot by the arrowed solid lines. Let us treat the case in which a critical stress $\tau_F^c > \tau_F$ is needed to nucleate the fault. Initially, the contact pressure p_0 increases without slip along branch (1), at $u = 0$. At a critical pressure $p_0 = p_F^c$ a fault pops in unstably along branch (2), until the upper equilibrium line for forward slip is intersected. Note that in the absence of a critical nucleation condition the fault would initiate stably at the intercept pressure $p_0 = \tau_F/(\beta_F - \alpha_F\mu_F) = p_F < p_F^c$, i.e. without pop-in. Further increase in contact pressure to a maximum value $p_0 = p_0^*$ causes slip to continue stably along branch (3). Now suppose we unload at some displacement $u^* < u_0$. The system traverses branch (4) at $u^* = [(\beta_F - \alpha_F\mu_F)p_0^* - \tau_F]/\kappa =$ constant from equation (6a). Along this unloading branch the fault shear stress $\sigma_F^S = \kappa u^*$ remains constant. At intersection of branch (4) with the u axis at $p_0 = 0$ the system is fully unloaded, so (unless we reverse the contact pressure, i.e. exert an adhesive "contact tension") we can not satisfy equation (6b) for reverse slip. Reloading along (5) then retraces (4), and all further cycles are constrained to this vertical branch. In summary, the fault exerts a monotonically increasing shear stress $\sigma_F^S = \kappa u$ during the loading half-cycle and a persistent shear stress $\sigma_F^S = \kappa u^*$ during (and after) the unloading half-cycle.

Note in Fig. 7 that there is hysteresis in the first cycle, but not in subsequent cycles. The latter kind of hysteresis may occur at "overloaded" contacts, such that the displacement at maximum load satisfies the condition $u^* > u_0$, leading to reverse slip along portion of the lower inclined line to $p_0 = 0$ during the unload half-cycle. Note that reverse slip would also occur if the cohesion were to be zero, i.e. $\tau_F = 0$ in equation (6), regardless of the maximum load, because then both the forward and backward slip lines would intersect the origin in Fig. 7.

4. *K*-FIELD ANALYSIS OF MICROCRACK DEVELOPMENT

Consider now the evolution of a microcrack FC from an edge F of the shear fault FF in Fig. 5. The problem of crack initiation from sliding shear cracks in confining triaxial compressive fields has been considered at some length by the rock mechanics community. Fracture mechanics treatments have been presented by Horii and Nemat-Nasser [28] and Ashby and Hallam [29], specifically for systems with preexisting faults. A characteristic feature of the microfracture in those cases is a highly stabilized extension at all stages of evolution to "failure", on planes closely normal to the least compressive of the principal stresses. In the case of alumina, it is necessary to allow for a potential initiation instability from twin pop-in. The pop-in problem bears striking similarities to that of crack initiation from shear faults in Vickers indentation fields [24], and it is the relatively straightforward stress-intensity factor approach of that analysis that we adopt here.

4.1. Crack-plane stresses

The initial microcrack increment will be governed by the near field associated with the shear fault, and will search for a path of maximum local tension. Ideally, for $\Psi = 45°$ in Fig. 5 (orientation for maximum shear on fault), this initial path corresponds to $\theta = 70.5°$ [29]. As the microcrack extends, it becomes influenced more strongly by the far-field contact stresses; the optimum orientation for maximum tension, again at $\Psi = 45°$, is then $\theta = 45°$. In reality, the fault may be constrained by crystallography at more unfavorable orientations, i.e. $\Psi \neq 45°$. Similarly, the microcrack may be constrained to extend along a grain or interphase boundary within the local shear-fault field, and therefore will not necessarily follow principal stress trajectories. Hence, in general, the microcrack segment will experience both modes I and II (and III, for that matter).

Once the crack path is established, the fracture mechanics are completely determined by the stresses from the contact field plus any internal stresses acting along that path. On the closed-fault (F) segment FF in Fig. 5, resolved normal (compressive) and shear contact-field stresses $\sigma(\Psi)$ and $\tau(\Psi)$ are defined in equations (1a) and (1b), respectively. The key stress that determines subsequent fracture extension during a full load–unload cycle is the *net* shear stress in equation (4a)

$$\sigma_F^S = (\beta_F - \alpha_F\mu_F)p_0 - \tau_F, \text{ (loading)} \qquad (7a)$$

$$\sigma_F^S = (\beta_F - \alpha_F\mu_F)p_0^* - \tau_F, \text{ (unloading–reloading)} \qquad (7b)$$

recalling that $\alpha_F = -\sigma(\Psi)/p_0$, $\beta_F = |\tau(\Psi)|/p_0$, and p_0^* the contact pressure at maximum loading, with $\sigma_F^S > 0$ always. We note that σ_F^S in equation (7b) remains constant during the unloading and any reloading half-cycles.

Similarly, for the extended open-microcrack (M) segment FC in Fig. 5, resolved contact-field stresses $\sigma(\Psi - \theta)$ and $\tau(\Psi - \theta)$ are defined in equation (2). Thus, normal stresses

$$\sigma_M^N = \sigma(\Psi - \theta) = -\alpha_M p_0 \qquad (8)$$

act throughout the loading–unloading cycle, with $\alpha_M = -\sigma(\Psi - \theta)/p_0$ another positive coefficient [cf. equation (3)]. Since this stress component exerts its maximum constraint at peak loading, the cracks will extend during unloading as well as loading, and conversely close during any reloading. Any shear stresses on the otherwise extensile microcrack are again expressible in the form [25]

$$\sigma_M^S = (\beta_M - \alpha_M\mu_M)p_0 - \tau_M, \text{ (loading–unloading)} \quad (9a)$$

$$\sigma_M^S = (\beta_M + \alpha_M\mu_M)p_0 + \tau_M, \text{ (reloading)} \quad (9b)$$

with positive coefficient $\beta_M = |\tau(\Psi - \theta)|/p_0$, crack-interface sliding friction coefficient μ_M and shear "cohesion" stress τ_M [cf. equation (5)]; again, it is required that $\sigma_M^S > 0$ for sliding. As with coefficients α_F and β_F in equations (2) and (3), invariance of α_M and β_M in equations (8) and (9) is contingent on reversibility of the stress field.

In addition, the extensile microcracks in noncubic polycrystals and two-phase materials are subject to thermal expansion mismatch stresses σ_R.

4.2. Stress–intensity factors for Mode I extension

In this section we make simplifying assumptions concerning the fault-microcrack geometry in Fig. 5, to minimize mathematical complexity. Thus in our stress-intensity factors we ignore the deflection of the microcrack from the fault plane by treating the system as a planar penny crack with radial coordinate r, radius $C = c + l/2$, subjected to stress σ_F^S [equation (7)] over $0 \leqslant r \leqslant l/2$ plus stresses σ_M^S, σ_M^N [equations (8, 9)] and σ_R over $l/2 \leqslant r \leqslant C$. Also, we choose the configuration that maximizes the contact field shear on the fault, $\Psi = 45°$, and tension on the developed microcrack, $\theta = 45°$; in this ideal case the shear stress σ_M^S in equation (9) is zero (see below), so the microcrack extends in pure mode I. On the other hand, recognizing that the σ_M^S term may be an essential element of fatigue (e.g. from frictional attrition at the sliding crack interface—Section 6), provision remains in the formalism of Sections 3 and 4 for a more general, mixed-mode analysis.

These geometrical simplifications allow us to calculate the α and β coefficients in the stress terms of Section 4.1. Inserting $\Psi = 45°$ in equation (1) yields fault stresses $\sigma(\Psi) = \frac{1}{2}(\sigma_1 + \sigma_3)$ and $\tau(\Psi) = \frac{1}{2}(\sigma_1 - \sigma_3)$; similarly, inserting $\Psi = 45° = \theta$ in equation (2) yields microcrack stresses $\sigma(\Psi - \theta) = \sigma_1$ and $\tau(\Psi - \theta) = 0$. Now we are concerned with the values of these stresses in the subsurface damage zone, specifically at the point of maximum shear stress at depth $0.5a$ beneath the contact center and for Poisson's ratio $\nu = 0.22$ for alumina. We find $\sigma_1 = -0.25p_0$ [Fig. 4(a)] and $\sigma_3 = -0.74p_0$ [Fig. 4(b)] at this point, yielding $\alpha_F = -\sigma(\Psi)/p_0 = 0.74$ and $\beta_F = |\tau(\Psi)|/p_0 = 0.49$, $\alpha_M = -\sigma(\Psi - \theta)/p_0 = 0.25$ and $\beta_M = |\tau(\Psi - \theta)|/p_0 = 0$. Since negative values of σ_M^S are inadmissable in equation (9a), the zero value of β_M guarantees mode I extension.

To compute K-fields for the extensile microcrack in the domain $C > l/2$, $c > 0$, we resort to standard relations for penny cracks subjected to crack-plane stress distributions $\sigma(r)$ [11, 42]. We obtain the following stress-intensity factors [24]:

(i) Shear-fault stress contribution. The stress σ_F^S [equation (7)] acting uniformly over $0 \leqslant r \leqslant l/2$ on the fault segment contributes

$$K_F(C, l) = \sigma_F^S l^{1/2} f_F(C/l) \qquad (10)$$

where the crack-size dependence is contained wholly in the dimensionless function [24, 42]

$$f_F(C/l) = 2(C/\pi l)^{1/2}\{[1 - (1 - l^2/4C^2)^{1/2}] - [\nu/(2-\nu)][1 - (1 - l^2/4C^2)^{3/2}]\}. \qquad (11)$$

Note in the limit of large extension, $C \gg l/2$, we have $K_F = [(1 - 2\nu)/2\pi^{1/2}(2 - \nu)]\sigma_F^S l^2/C^{3/2}$, i.e. the system is highly stable with the same $C^{-3/2}$ crack size dependence as indentation cracks [11].

(ii) Microcrack–stress contribution. The uniform contact field stresses σ_M^N [equation (8)] acting over $l/2 \leqslant r \leqslant C$ on the microcrack segment contributes

$$K_M(C, l) = \sigma_M^N l^{1/2} f_M(C/l) \qquad (12)$$

with the dimensionless crack size function [24]†

$$f_M(C/l) = 2(C/\pi l)^{1/2}(1 - l^2/4C^2)^{1/2}. \qquad (13)$$

Note that K_M is zero for the first microcrack growth increment at $C = l/2$, $c = 0$. Thereafter, since σ_M^N in equation (8) is negative in the damage zone, K_M increasingly constrains the extension.

(iii) Residual-stress contribution. For cracks initiating on a grain boundary facet under the action of a uniform thermal expansion mismatch stress σ_R we have

$$K_R(C, l) = \sigma_R l^{1/2} f_R(C/l) \qquad (14)$$

in which the crack-size function

$$f_R(C/l) = 2(C/\pi l)^{1/2}(1 - l^2/4C^2)^{1/2} \qquad (15)$$

has the same form as equation (13). As with K_M, the contribution K_R is zero for the first microcrack growth increment. At $C \gg l/2$ we have $K_R = (2/\pi^{1/2})\sigma_R C^{1/2}$, so for tensile facets ($\sigma_R > 0$) K_R is a destabilizing influence in the extension.

The net K-field for microcrack extension is therefore the superposition of the contributions in equations (10–15)

$$\begin{aligned} K_*(C/l) &= K_F + K_M + K_R \\ &= \sigma_F^S l^{1/2} f_F(C/l) + \sigma_M^N l^{1/2} f_M(C/l) \\ &\quad + \sigma_R l^{1/2} f_R(C/l). \end{aligned} \qquad (16)$$

Extension then occurs when the crack-tip K-field is just sufficient to overcome the intrinsic (grain or interphase boundary) toughness of the material, i.e. $K_* = T_0$. Given that the dimensionless $f(C/l)$ functions are invariant for geometrically similar microstructures, the quantity $l^{1/2}$ emerges as the key scaling quantity in the K-field formalism.

5. EFFECT OF GRAIN SIZE ON MICROCRACK INITIATION AND EXTENSION IN ALUMINA

Allusion has been made to the role of grain size in determining the microfracture damage in polycrystalline materials, in both the experimental

---

†Calculable directly from the standard stress-intensity factor relation for penny cracks with distributed stresses $\sigma(r)$ [11]

$$K(C) = 2/(\pi C)^{1/2} \int_0^C r\sigma(r)\mathrm{d}r/(C^2 - r^2)^{1/2}.$$

observations referred to in Section 2.1 (e.g. Figs 2 and 3) and the theoretical formalism just described in Section 4.2 [e.g. $l^{1/2}$ term in equation (16)]. In the present section we demonstrate the capacity of our model to provide quantitative information on this critical microstructural scaling effect, with specific reference to alumina.

Accordingly, along with the calibrated α and β coefficients from Section 4.2, we assign the following quantities for insertion into the fracture mechanics analysis, from independent data on alumina:

(i) Grain boundary toughness $T_0 = 2.75$ MPa.m$^{1/2}$, from indentation-strength tests [15]; and thermal expansion mismatch stress $\sigma_R = 200$ MPa, from spectroscopic measurements [41].

(ii) Critical contact stress $p_F^C = 5.0$ GPa (see Fig. 7), corresponding to the nucleation pressure at which faulting is first evident in indentation stress–strain curves (Fig. 1), optical microscopy (Fig. 2) and acoustic emission (Fig. 3) [18].

(iii) Fault intercept quantity $p_F = \tau_F/(\beta_F - \alpha_F \mu_F)$ from Section 3 (see Fig. 7), to evaluate σ_F^S in equation (7). We choose $p_F = 3.0$ GPa to provide sensible values below for the fully extended microcrack dimensions (note that $p_F < p_F^C$, as required in Fig. 7). If we assume that the twinning in alumina is governed entirely by a critical cohesion stress, so that $\mu_F = 0$, we evaluate $\tau_F = \beta_F p_F = 1.4$ GPa.

It is acknowledged that these parameter evaluations are approximate, and that the fracture mechanics formalism embodies many assumptions, so the numerical accuracy of the calculations are open to a degree of uncertainty.

In Fig. 8 we plot the function $K_*(c)$ from equation 16 [in conjunction with equations (7–15)] for a selected alumina grain size $l = 35\,\mu$m, incrementing p_0 to a peak $p_0^* = 10$ GPa in a complete load–unload cycle (cf. Fig. 1). Extension occurs along the horizontal equilibrium line $K_* = T_0$. Because of the dominating influence of the K_F and K_M terms at small c in equation (16), the microcrack is stabilized (i.e. $dK_*/dc < 0$), most strongly in the loading half-cycle. However, at large c the K_R term becomes dominant in equation (16), and the $K_*(c)$ function begins to rise on approaching the final unload state. This indicates that the crack configuration is approaching an instability configuration. If such a configuration were to be achieved (e.g. by admitting water to the subsurface fault–microcrack to promote subcritical extension), the unloaded microcrack would extend unstably into the surrounding microstructure. The material would then be on the verge of spontaneous bulk microfracture, and its structural integrity would be contingent on the arrest of individual microcracks at adjacent grain facet bridges [11, 16].

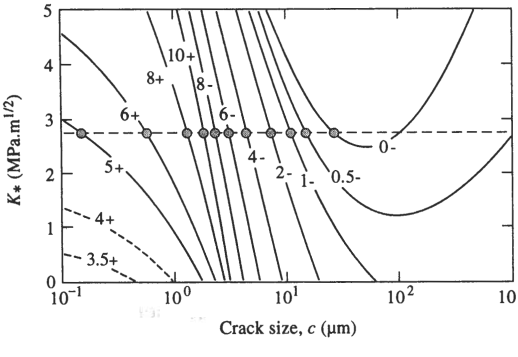

Fig. 8. Plots of function $K_*(c)$ in equation (16) for fault-generated microcracks in alumina of grain size $35\,\mu$m, for indicated values of contact pressure p_0 (GPa) during load (+) and unload (−) half-cycles. Equilibrium condition determined by intersection with horizontal dashed line, representing grain boundary toughness T_0. Dashed curves at contact pressure $p_0 < p_F^C = 5.0$ GPa indicate region prior to fault initiation. At p_F^C microcrack pops in, and thereafter grows stably along $K_* = T_0$ (circles).

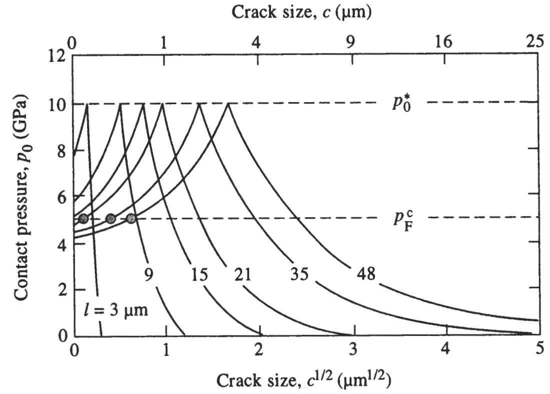

Fig. 9. Plots of function $p_0(c)$ for equilibrium cracks ($K_* = T_0$) for alumina at specified grain sizes (cf. Fig. 3). Horizontal dashed line denotes critical fault pressure $p_F^C = 5.0$ GPa. Intercepts at $c = 0$ represent minimum contact pressures p_M [equation (17)] for extension of existing miocrocrack. For grain sizes $l < 20\,\mu$m, $p_M > p_F^C$, and extension occurs stably at $p_0 = p_M$; for $l > 20\,\mu$m, $p_M < p_F^C$, and microcracks must first pop in at $p_0 = p_F^C$ before stable extension occurs.

It is important to remember that our model presumes the existence of a shear fault. In reality, a microcrack cannot form unless a fault nucleates first, at $p_0 = p_F^C = 5.0$ GPa. At p_F^C the microcrack pops in spontaneously, to $c \approx 0.2\,\mu$m for our $35\,\mu$m grain size alumina in Fig. 8. As the pressure continues to increase beyond p_F^C the microcrack extends stably, to $c \approx 3\,\mu$m at $p_0 = p_0^* = 10$ GPa. On unloading, the microcrack continues in stable growth, at an ever-increasing rate, to its final size $c \approx 23\,\mu$m at $p_0 = 0$, i.e. less than one grain facet for this material.

The grain size effect is more clearly represented by $p_0(c)$ curves for equilibrium microcrack extension, obtainable either directly from equation (16) [again together with equations (7–15)] at $K_* = T_0$ or from intersection points along the horizontal dashed line in Fig. 8. We show such a plot in Fig. 9 for alumina at several grain sizes (cf. Fig. 3), for peak pressure $p_0^* = 10$ GPa. Stable branches during both half-cycles are again evident. The dashed line at

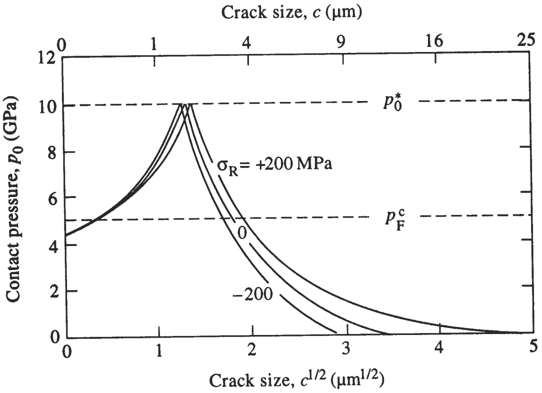

Fig. 10. Plots of $p_0(c)$ for equilibrium cracks for alumina of grain size 35 μm, showing effect of residual thermal expansion mismatch stress σ_R.

$p_0 = p_F^C = 5.0$ GPa represents the critical stress for fault nucleation, independent of grain size l. The intercept $p_0(c) = p_M$ at $c = 0$ ($C = l/2$) represents the minimum pressure for microcrack extension, and *does* depend on l,

$$p_M(l) = p_F(\pi^{1/2}T_0/2\tau_F l^{1/2} - 1). \qquad (17)$$

At grain sizes $l < 20\ \mu$m in Fig. 9, p_M lies above the threshold p_F^C line; in this region p_0 must be increased above this line before a microcrack can extend. When extension does occur, it is stable. At grain sizes $l > 20\ \mu$m, p_M falls below p_F^C, so no fault exists from which extension can occur; in this region, the loading must first be increased to the threshold level. At threshold the microcrack pops in along the $p_0 = p_F^C$ line to the first branch of the $p_0(c)$ curve, producing constrained flaws of dimension $c \approx 0.5\ \mu$m for the largest grain size l in Fig. 9. Through the remainder of the loading–unloading cycle, extension is again stable, with extension to $c > 100\ \mu$m at largest l. We note that the scale of microcrack pop-in increases monotonically with grain size above $l \approx 20\ \mu$m in Fig. 9, consistent with the acoustic emission data in Fig. 3.

In Fig. 10 we plot the $p_0(c)$ curve for alumina at $l = 35\ \mu$m using thermal mismatch stresses $\sigma_R = 200$, 0, and -200 MPa. We note that while σ_R has no bearing on the value of the intercept stress p_M at $c = 0$, it has a pronounced influence on the ultimate microcrack extension. The contrast between final crack sizes $c \approx 23\ \mu$m at the tensile facet and $c \approx 8\ \mu$m at the compressive facet serves to emphasize the important role of internal stresses in the damage susceptibility.

6. DISCUSSION

Hertzian contact presents itself as a powerful test procedure for investigating fundamental deformation-assisted damage properties of otherwise highly brittle polycrystalline materials. Our damage model is based on microcrack extension from stress concentrations at constrained "shear faults". Such faults account for the subsurface "plastic" deformation observed in indentation stress–strain responses, micrographic sections, and acoustic emission records. These experimental elements have been demonstrated for a monophase alumina ceramic in Figs 1–3. In alumina, the shear faults are primarily associated with the activation of intra-grain twinning. In brittle ceramics in general, the stresses required to activate analogous shear faults are characteristically high, often approaching the cohesive shear strength of the material. In glass, shear faults occur along principal shear stress trajectories [23, 35, 43]. In single crystals, e.g. silicon [44] or sapphire [45, 46], they result from "block slip" on low-index crystallographic planes. In multiphase composites [19], including rocks [25, 27], slippage occurs on some incipient weak interface associated with microstructural defects, e.g. sliding grain or interphase boundary facets. In polycrystalline ceramics any one or more of these processes may be active as incipient faults.

The closed-fault model outlined in Section 3 captures the generic essence of the precursor deformation process. While retaining the traditional friction and cohesion stress descriptions of shear-activated faulting in rock mechanics [25], our model allows for fault pop-in by incorporating a fault nucleation stress. It also allows for an additional, constraining effect of the matrix on individual grains within the subsurface Hertzian contact field in Fig. 4. We recall from Fig. 6 that the fault is most commonly expected to be active only in the first load half-cycle, i.e. along branch (2) in Fig. 6. Continued hysteretic activity during subsequent unloading and reloading half-cycles is predicted only in overloaded contacts.

The principal focus of the model is the extension of microcracks from the closed shear faults in the constraining subsurface compressive field, again in the spirit of traditional rock mechanics but here expressed in terms of the K-field formalisms previously used to describe radial crack initiation in sharp-indenter contacts [23, 24, 33, 43, 47, 48]. In its most general form, the model enables one to describe a continuing crack evolution through sequential load–unload contact cycles, with due allowance for a mode II component. However, our specific treatment in Sections 4 and 5 defers consideration of the mode II terms, in the interest of simplicity. The model predicts microcrack pop-in during the loading half-cycle (required to account for acoustic emission data) and enhanced stable extension during the unloading half-cycle, highlighting the stabilizing influence of the compressive field.

We have alluded to the relevance of contact damage to several mechanical properties of brittle ceramics, including damage accumulation [29], material removal and wear [49, 50], and strength degradation [17, 19]. But perhaps the property of greatest practical significance is *fatigue*, e.g. in contact bearings and dental–ceramic restorations

[51]. Experimentally, strong contact fatigue effects have been reported in cyclic tests on coarse-grain aluminas [17]. In such fatigue phenomena, the inbuilt provision for frictional tractions in the crack-plane stresses of Section 4.1, at both the fault and microcrack interfaces, is indispensable. Accordingly, we foreshadow two potential contributions to contact fatigue:

(i) *Individual microcrack evoluation*. Sliding crack interfaces can lead to progressive frictional degradation or wear in continual reversed loading. Direct evidence for interfacial attrition has been reported in the accumulation of wear products and debris at cracked grain boundary interfaces in alumina [30, 52, 53] and rocks [27, 54]. With diminishing values of the friction μ and τ terms in the shear stresses σ_F^S and σ_M^S in Section 4.1, the final crack sizes in Figs 8 and 9 become subject to progressive extension with number of cycles. This raises the prospect of interaction and coalescence of neighboring microcracks [29], leading ultimately to fragmentation [17]. Any such process will be enhanced by the accumulation of debris at the sliding crack interfaces [30, 52].

(ii) *Deformation zone expansion*. It is well known from rock mechanics that the compliance of specimens in compression loading increases significantly with the introduction of closed, but sliding, microcracks [25]. As extending microcracks begin to interact with their neighbors in a confined contact field, the local compliance within the damage zone will increase, with consequent stress transfer to the immediately surrounding matrix. Accordingly, the adjacent matrix grains will bear more of the transmitted contact load, and will themselves become susceptible to faulting. The deformation zone, and thence the microcrack density, will therefore spread outward, exacerbating the fatigue process.

Finally, the fracture mechanics analysis has important implications concerning material characteristics in design:

(i) *Grain size*. As indicated in Section 5, grain size is a critical element in the microcrack evolution, most dramatically in the initiation. This enhancement of fracture susceptibility with microstructural scaling, illustrated dramatically by the contact damage in alumina ceramics (e.g. Figs 2 and 3 [18]), is a widespread phenomenon in brittle fracture [11, 55, 56]. The connotation in the special context of ceramics processing is that minimal susceptibility to damage accumulation requires refinement of mean grain size. In reality, for any given material there may be a *distribution* of grain sizes (as well as of crystal misorientations), so the transition may not be abrupt, especially in inhomogeneous stress fields like that in Fig. 4. The result is then a progressive accumulation of microcracks as the load is increased at given nominal grain size, or as grain size is increased at prescribed load [18]. Hence, not only grain size, but also grain-size *variation*, is subject to refinement.

(ii) *Residual thermal mismatch stress*. Noncubic and two-phase ceramics are subject to thermal expansion and other mismatch stresses at intergrain facets. The tensile component of these stresses greatly enhances final microcrack extension within the contact field. Hence it would appear that microstructures with large mismatch stresses will be most susceptible to contact damage. On the other hand, countervailing compressive stresses at adjacent bridging facets constitute a most effective route to effective crack–interface bridging in the long-crack region [11, 15]. We have omitted considerations of bridging tractions from our analysis, on the grounds that the individual microcracks remain confined to a grain facet or so. However, bridging stresses will become important in the secondary stages of multiple crack coalescence and material removal [29].

(iii) *Nature of strength-degrading flaws*. Polycrystalline ceramics inevitably contain a population of pre-existing *extrinsic* flaws, e.g. from the processing and surface treatments. However, in ceramics like alumina the flaws leading to microfracture may be *activated* by the very contact event itself, via the shear faulting process. Insofar as this shear faulting process occurs at a well-defined contact stress independent of grain size (recall p_F^C in Fig. 9), such flaws are governed by material-*intrinsic* factors. Hence preexisting flaws may be expected to play only a secondary role in the micromechanics of damage accumulation (although they might well exert a dominant influence near the critical grain size for *spontaneous* general microcracking [11, 49, 50]). There is the strong suggestion here that, contrary to common expectation, initial flaw state may not be a decisive factor in determining the resistance of polycrystalline ceramics to contact fatigue.

Acknowledgements—Funding for this study was provided by the U.S. Air Force Office of Scientific Research. Special financial support for FG from the Ministerio de Educación Y Ciencia (DGICYT), Spain, and from NIST, is gratefully acknowledged.

REFERENCES

1. H. Hertz, *Hertz's Miscellaneous Papers*, Chaps 5, 6. Macmillan, London (1896).
2. F. C. Roesler, *Proc. Phys. Soc. Lond.* **B69,** 981 (1956).
3. F. C. Frank and B. R. Lawn, *Proc. R. Soc.* **A299,** 291 (1967).
4. B. R. Lawn, *J. appl. Phys.* **39,** 4828 (1968).
5. F. B. Langitan and B. R. Lawn, *J. appl. Phys.* **40,** 4009 (1969).
6. B. R. Lawn and T. R. Wilshaw, *J. Mater. Sci.* **10,** 1049 (1975).
7. A. G. Evans and T. R. Wilshaw, *Acta metall.* **24,** 939 (1976).
8. B. R. Lawn and D. B. Marshall, *Fracture Mechanics of Ceramics* (edited by R. C. Bradt, D. P. H. Hasselman and F. F. Lange), Vol. 3, p. 205. Plenum Press, New York (1978).
9. M. V. Swain and B. R. Lawn, *Physica status solidi* **35,** 909 (1969).

10. M. V. Swain and J. T. Hagan, *J. Phys. D, Appl. Phys.* **9,** 2201 (1976).
11. B. R. Lawn, *Fracture of Brittle Solids*, 2nd edn. Cambridge Univ. Press (1993).
12. R. Knehans and R. Steinbrech, *Science of Ceramics* (edited by P. Vincenzini), Vol. 12, p. 613. Ceramurgica, Imola, Italy (1983).
13. P. L. Swanson, C. J. Fairbanks, B. R. Lawn, Y.-W. Mai and B. J. Hockey, *J. Am. Ceram. Soc.* **70,** 279 (1987).
14. S. J. Bennison and B. R. Lawn, *J. Mater. Sci.* **24,** 3169 (1989).
15. S. J. Bennison and B. R. Lawn, *Acta metall.* **37,** 2659 (1989).
16. P. Chantikul, S. J. Bennison and B. R. Lawn, *J. Am. Ceram. Soc.* **73,** 2419 (1990).
17. F. Guiberteau, N. P. Padture, H. Cai and B. R. Lawn, *Phil. Mag. A.* **68,** 1003 (1993).
18. F. Guiberteau, N. P. Padture and B. R. Lawn, *J. Am. Ceram. Soc.* In press.
19. H. Cai, M. A. Stevens Kalceff and B. R. Lawn, *J. Mater. Res.* In press.
20. A. N. Stroh, *Adv. Phys.* **6,** 418 (1957).
21. A. H. Cottrell, *Trans. metall. Soc. A.I.M.E.* **212,** 192 (1958).
22. N. J. Petch, *Fracture* (edited by H. Liebowitz), Vol. 1, Chap. 5. Academic Press, New York (1968).
23. B. R. Lawn, T. P. Dabbs and C. J. Fairbanks, *J. Mater. Sci.* **18,** 2785 (1983).
24. S. Lathabai, J. Rödel, B. R. Lawn and T. P. Dabbs, *J. Mater. Sci.* **26,** 2157 (1991).
25. J. C. Jaeger and N. G. W. Cook, *Fundamentals of Rock Mechanics*, Chapman & Hall, New York (1971).
26. M. S. Paterson, *Experimental Rock Deformation—The Brittle Field.* Springer, Berlin (1978).
27. R. L. Kranz, *Tectonophysics* **100,** 449 (1983).
28. H. Horii and S. Nemat-Nasser, *J. Geophys. Res.* **90,** 3105 (1985).
29. M. F. Ashby and S. D. Hallam, *Acta metall.* **34,** 497 (1986).
30. L. Ewart and S. Suresh, *J. Mater. Sci.* **22,** 1173 (1987).
31. S. Suresh and J. R. Brockenbrough, *Acta metall.* **36,** 1455 (1988).
32. S. Suresh, *Fatigue of Materials.* Cambridge Univ. Press (1991).
33. J. T. Hagan, *J. Mater. Sci.* **14,** 2975 (1979).
34. J. T. Hagan, *J. Mater. Sci.* **14,** 462 (1979).
35. J. T. Hagan, *J. Mater. Sci.* **15,** 1417 (1980).
36. S.v.d. Zwagg, J. T. Hagan and J. E. Field, *J. Mater. Sci.* **15,** 2965 (1980).
37. T. P. Dabbs, C. J. Fairbanks and B. R. Lawn, *Methods for Assessing the Structural Reliability of Brittle Materials* (edited by S. W. Freiman and C. M. Hudson), p. 142. A.S.T.M. Special Tech. Publ. 844, Philadelphia, Pa (1984).
38. D. Tabor, *Hardness of Metals.* Clarendon, Oxford (1951).
39. K. L. Johnson, *Contact Mechanics*, Cambridge Univ. Press (1985).
40. T. R. Wilshaw, *J. Phys. D, Appl. Phys.* **4,** 1567 (1971).
41. J. E. Blendell and R. L. Coble, *J. Am. Ceram. Soc.* **65,** 174 (1982).
42. H. Tada, P. Paris and G. R. Irwin, *The Stress Analysis of Cracks Handbook.* Del Research, St. Louis (1985).
43. J. T. Hagan and M. V. Swain, *J. Phys. D* **11,** 2091 (1978).
44. M. J. Hill and D. J. Rowcliffe, *J. Mater. Sci.* **9,** 1569 (1974).
45. B. J. Hockey and B. R. Lawn, *J. Mater. Sci.* **10,** 1275 (1975).
46. H. M. Chan and B. R. Lawn, *J. Am. Ceram. Soc.* **71,** 29 (1988).
47. B. R. Lawn and A. G. Evans, *J. Mater. Sci.* **12,** 2195 (1977).
48. S. Lathabai, J. Rödel, B. R. Lawn and T. P. Dabbs, *J. Mater. Sci.* **26,** 2313 (1991).
49. S.-J. Cho, B. J. Hockey, B. R. Lawn and S. J. Bennison, *J. Am. Ceram. Soc.* **72,** 1249 (1989).
50. S.-J. Cho, H. Moon, B. J. Hockey and S. M. Hsu, *Acta metall. mater.* **40,** 185 (1992).
51. D. G. Grossman, *Proc. Int. Symp. on Computer Restorations* (edited by W. H. Mörmann), p. 103. Quintessence, Chicago, Ill. (1991).
52. S. Lathabai, J. Rödel and B. R. Lawn, *J. Am. Ceram. Soc.* **74,** 1340 (1991).
53. R. H. Dauskardt, *Acta metall. mater.* **41,** 2765 (1993).
54. M. L. Batzle, G. Simmons and R. W. Siegfried, *J. Geophys. Res.* **85,** 7072 (1980).
55. B. R. Lawn and D. B. Marshall, *J. Am. Ceram. Soc.* **62,** 347 (1979).
56. K. E. Puttick, *J. Phys. D, Appl. Phys.* **12,** L19 (1979).